Quantified abundance of magnetofossils at the Paleocene–Eocene boundary from synchrotron-based transmission X-ray microscopy

Huapei Wang[a], Jun Wang[b], Yu-chen Karen Chen-Wiegart[b], and Dennis V. Kent[c,d,1]

[a]Earth, Atmospheric and Planetary Sciences, Massachusetts Institute of Technology, Cambridge, MA 02139; [b]Photon Sciences Directorate, Brookhaven National Laboratory, Upton, NY 11973; [c]Earth and Planetary Sciences, Rutgers University, Piscataway, NJ 08854; and [d]Lamont–Doherty Earth Observatory, Columbia University, Palisades, NY 10964

Contributed by Dennis V. Kent, September 2, 2015 (sent for review June 19, 2015; reviewed by Michael Winklhofer)

The Paleocene–Eocene boundary (~55.8 million years ago) is marked by an abrupt negative carbon isotope excursion (CIE) that coincides with an oxygen isotope decrease interpreted as the Paleocene–Eocene thermal maximum. Biogenic magnetite (Fe_3O_4) in the form of giant (micron-sized) spearhead-like and spindle-like magnetofossils, as well as nano-sized magnetotactic bacteria magnetosome chains, have been reported in clay-rich sediments in the New Jersey Atlantic Coastal Plain and were thought to account for the distinctive single-domain magnetic properties of these sediments. Uncalibrated strong field magnet extraction techniques have been typically used to provide material for scanning and transmission electron microscopic imaging of these magnetic particles, whose concentration in the natural sediment is thus difficult to quantify. In this study, we use a recently developed ultrahigh-resolution, synchrotron-based, full-field transmission X-ray microscope to study the iron-rich minerals within the clay sediment in their bulk state. We are able to estimate the total magnetization concentration of the giant biogenic magnetofossils to be only ~10% of whole sediment. Along with previous rock magnetic studies on the CIE clay, we suggest that most of the magnetite in the clay occurs as isolated, near-equidimensional nanoparticles, a suggestion that points to a nonbiogenic origin, such as comet impact plume condensates in what may be very rapidly deposited CIE clays.

Paleocene–Eocene thermal maximum | New Jersey Atlantic Coastal Plain | impact plume condensate | Marlboro Clay | Ocean Drilling Program Leg 174AX

The Paleocene–Eocene boundary is marked by an abrupt global negative carbon isotope excursion (CIE) in both marine and continental carbon reservoirs (1, 2) that coincides with an oxygen isotope decrease that is interpreted as a rapid global warming event at ~55.8 million years ago, the Paleocene–Eocene thermal maximum (PETM) (3). The thick zone of anomalously high magnetization coincident with the CIE at the base of the Manasquan Formation (now known as the Marlboro Clay) was initially discovered in a cored section at Ancora (Ocean Drilling Program Leg 174AX) on the Atlantic Coastal Plain of New Jersey (4). Magnetic hysteresis measurements on the bulk sediment indicated that the anomalous high magnetization corresponds to an increased abundance of fine-grained magnetite with single-domain (SD)-like magnetic properties. Two other drill cores (Clayton and Bass River) show a similar association of high concentration of SD magnetite in a kaolinite-rich interval with minimum carbon isotope values and, with the Ancora site, form a transect across the New Jersey Atlantic Coastal Plain (5). Transmission electron microscopic (TEM) imaging on a redeposited thin layer of bulk clay from the CIE interval in the Clayton site resulted in finding only a handful of isolated nanoscale (~50 to ~70 nm) magnetite grains (5) because of the grains' low concentration, with distances between grains estimated to be ~20 times larger than their lengths in three-dimensional (3D) space (6). This unique magnetite nanoparticle-rich interval associated with the CIE on the New Jersey Atlantic Coastal Plain was suggested to have originated from impact plume condensates (5) in what now appears may have been very rapidly deposited (~1–3 cm/y) clays (7), providing circumstantial evidence for a major cometary impact at the onset of the CIE, which likely triggered the PETM (5, 8).

Subsequent studies have confirmed the anomalously high concentrations of SD-like material from the CIE clay from the Atlantic Coastal Plain, making these CIE sections the thickest dominated by SD magnetite recognized thus far in the stratigraphic record (9, 10). In these follow-up studies, scanning electron microscopic (SEM) and TEM observations on magnetically extracted materials revealed the presence of chains of magnetite crystals that strongly resembled magnetosomes of magnetotactic bacteria (MTB); this finding led to the conclusion that the SD-like magnetic properties of the CIE clays were predominantly of biogenic origin. However, quantitative analysis of the magnetic extraction procedure suggested that the extracted material accounts for only ~5% of the total magnetization (6). To further complicate the problem, SEM and TEM studies on the magnetic extracts also found giant micron-sized magnetofossils, including spearhead-like and spindle-like ones, inside the CIE clay across the New Jersey Atlantic Coastal Plain (11–13), and these magnetofossils were found to have SD-like magnetic properties, by electron holography, attributable to their distinct shapes (13). Using mainly SEM

Significance

The Paleocene–Eocene thermal maximum (PETM) is an abrupt global warming event that occurred at about 55.8 Ma and is closely linked to a large carbon isotope excursion. What caused the PETM is unresolved. An unusual abundance of single-domain magnetite particles in PETM sediments on the Atlantic Coastal Plain might represent condensates from a comet impact. Alternatively, the magnetic nanoparticles may be of biogenic origin. We are now able to quantify the concentration of those magnetic grains that are distinctly of biogenic origin using synchrotron-based transmission X-ray microscopy. These and related findings allow us to exclude magnetofossils as a significant source of magnetization of the PETM sediments and point to an impact condensate origin of the magnetite particles.

Author contributions: H.W. and D.V.K. designed research; H.W., J.W., and Y.-c.K.C.-W. performed research; H.W. and D.V.K. analyzed data; and H.W., J.W., and D.V.K. wrote the paper.

Reviewers included: M.W., Ludwig Maximilians University of Munich.

The authors declare no conflict of interest.

[1]To whom correspondence should be addressed. Email: dvk@rutgers.edu.

This article contains supporting information online at www.pnas.org/lookup/suppl/doi:10.1073/pnas.1517475112/-/DCSupplemental.

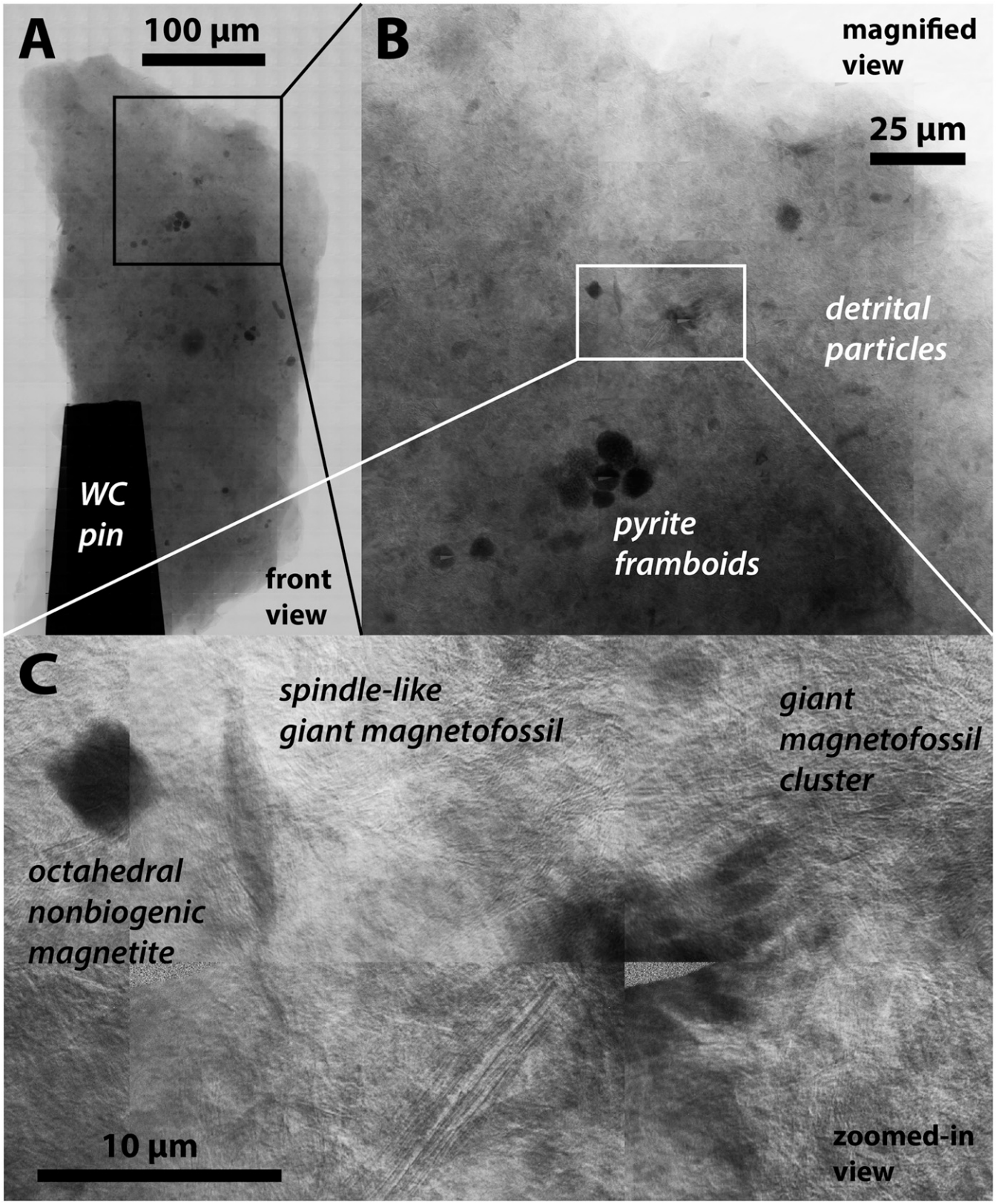

Fig. 1. (*A*) TXM mosaic scan of the front view of a submillimeter bulk CIE clay dust AN560.1-X1 in fast mode. (*B*) Slow mosaic mode scan of the boxed area in *A*. (*C*) Zoomed-in view of the boxed area in *B*.

or TEM with their limited fields of view (~micron) and shallow penetration depth (~100 nm), the absolute concentration of these biogenic magnetites could not be quantified, and thus the anomalously high magnetization of the CIE clay could not be ascribed to either mainly biogenic or nonbiogenic origins.

Results

In this study, we used a recently developed full-field hard X-ray ultrahigh-resolution (~30–50 nm without binning pixels) synchrotron-based transmission X-ray microscope (TXM) (14) with a field of view of 20 μm × 20 μm to study magnetite and other iron-rich minerals in bulk CIE clay (AN560.1 from 165.5 m depth of the Ancora core) from just above the onset of the CIE and the coincident high-magnetization layer (5, 6). In the front and side views of the TXM image of a submillimeter bulk CIE clay dust (AN560.1-X1) mounted on a tungsten carbide (WC) pin (Fig. 1 and Fig. S1), we can identify a variety of detrital iron minerals, as well as pyrite framboids of ~10-μm sizes and their clusters, a large ~5-μm nonbiogenic magnetite with its distinct octahedral crystal shape (15), a large ~10-μm spindle-like crystal that is likely to be an extraordinarily large giant magnetite magnetofossil, and also a cluster of spindle-like crystals of ~5–10 μm in size, which likely captures the general configuration of the creature that produced these giant magnetite crystals. Mosaic scans of four extra bulk clay dusts from AN560.1 (Fig. S2) have similar iron minerals as shown in AN560.1-X1. For several 20-μm-size cylindrical volumes that contain iron minerals within the bulk clay, we also conducted nanotomography to study the microstructure of the particles in three dimensions (Fig. S3 and Movies S1–S7), which helped us to further characterize the iron minerals using their crystal shapes.

We also scanned the magnetically extracted materials from the CIE clay sample (AN560.1) obtained in a previous study (6), which showed an intense increase of the concentration of iron-rich minerals (Fig. S4), whereas the TXM scan of the magnetically extracted residue of the CIE clay showed a certain decrease of iron mineral concentration (Fig. S5). To test the capability of the TXM to identify magnetite magnetofossils of ~1–2 μm or less, we conducted mosaic scans on a redeposited thin layer of the magnetically extracted materials (Fig. 2*A*). In this 100 μm × 100 μm area, we can identify many ~1–2-μm-size giant magnetofossils (e.g., Fig. 2 *B*–*F*) and estimate that there are many tens of spearhead-like and spindle-like biogenic magnetites. This is much more than that we can clearly identify from the TXM scans of the bulk submillimeter sized CIE clay dusts because the ~100- to

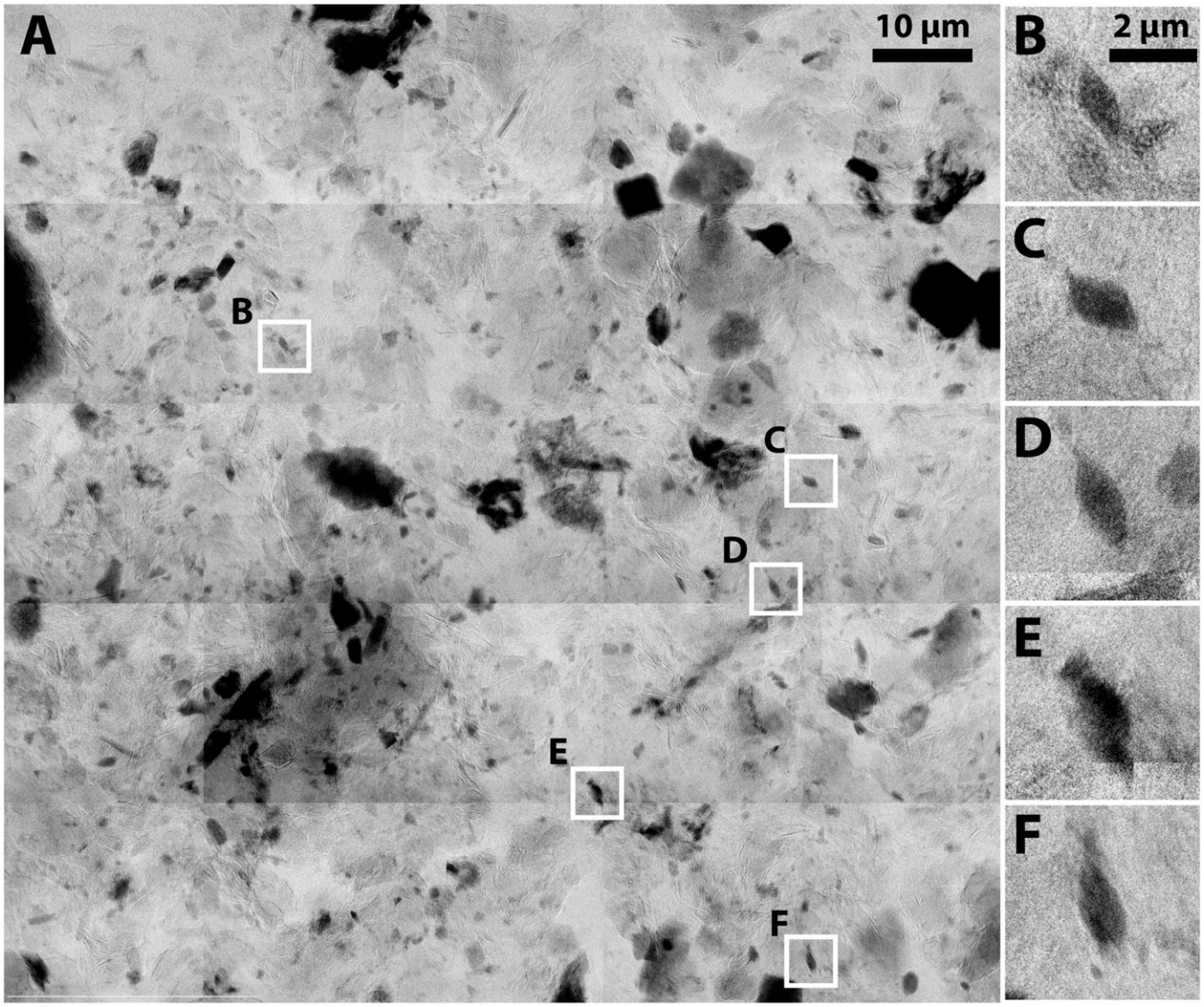

Fig. 2. (*A*) TXM mosaic scan of a thin layer of redeposited magnetically extracted materials from CIE clay sample AN560.1. (*B*–*F*) Examples of clearly identifiable ~1–2-μm-sized giant magnetofossils.

~200-μm thicknesses of the bulk clay dusts significantly reduce the contrast and clarity of the X-ray images.

Although the spatial resolution of the TXM is ~30–50 nm without binning pixels for a 20-μm × 20-μm field of view (14), the X-ray absorption from an individual ~50- to ~100-nm-sized nanoparticle is still too weak to produce a clear contrast to show the magnetosome chains produced by MTB or nonbiogenic isolated magnetite nanoparticles (Fig. 2). For the same reason, the magnetosomes in samples of a freeze-dried culture of MTB strain MV-1 (6, 16) are also not clearly observed by TXM (Fig. S6).

To clearly identify the giant magnetofossils and better estimate their concentration within the CIE clay, we redeposited known amount of the bulk CIE clay in a thin layer with an estimated average thickness of 4 μm on a 50-nm-thick silicon nitride (SN) window for ultrahigh-resolution TXM scans. After scanning a total area of 0.55 mm^2 by taking 1,370 TXM images, we identified ~50 giant magnetofossils, including spearhead-like and spindle-like ones (Fig. 3). Our X-ray images also provide opportunities to characterize their morphology. Fig. 4 shows the size and shape distribution of the giant magnetofossils identified by TXM in this study, as well as the magnetofossils (including MTB magnetosomes) identified by SEM and TEM in previous studies (9, 13). Because of the weak X-ray absorption from our sample and the limitation of spatial resolution of the TXM, we do not confidently observe the elongated prismatic magnetites or the MTB magnetosomes. Nevertheless, our TXM identified that spearhead-like and spindle-like giant magnetofossils inside the bulk clay generally have similar sizes and shapes as the ones previously identified by SEM or TEM. However, the magnetites observed by SEM or TEM are from magnetic extracts of the clay, which account for only 5% of its total magnetization (6), and thus not representing the entire magnetic assemblage of the bulk clay. This finding may be the reason that we find slightly larger scatter of the size and shape distribution of the giant magnetofossils in the bulk clay from our TXM study.

By knowing the exact amount of the bulk CIE clay that we scanned (2.2×10^{-3} mm^3 or 3.5 μg), we are able to calculate the saturation magnetization (M_s) contribution of the giant magnetofossils that we observed [based on magnetite $M_s = 92$ Am^2/kg (17)], which turns out to be 1.6×10^{-3} Am^2/kg or only about 10% of the M_s of the bulk CIE clay [1.5×10^{-2} Am^2/kg (5)].

Discussion

Our quantitative results show that the spearhead-like and spindle-like giant magnetofossils that are clearly identified in our TXM scans constitute only ~10% of the magnetic particles (by weight or volume) of the entire magnetization assemblage of the CIE clay. This would leave ~90% of the magnetization assemblage to be elongated prismatic magnetite crystals, magnetosome chains produced by MTB, and isolated nonbiogenic

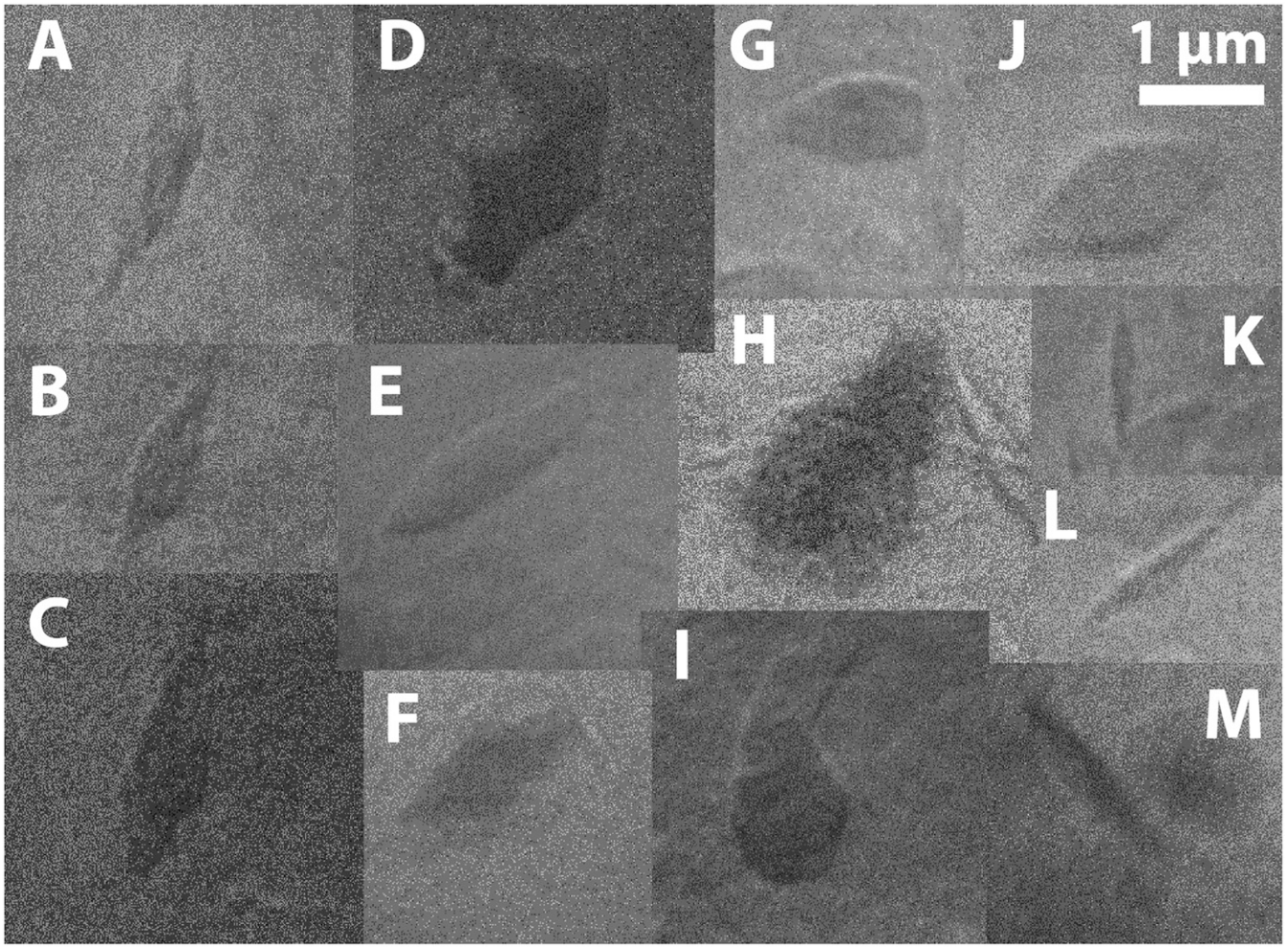

Fig. 3. TXM images of identifiable giant magnetofossils. (*A–C*) Spearhead-like magnetofossils. (*D–F*) Spearhead-like magnetofossils with buds. (*G–J*) Bullet-shaped spearhead-like magnetofossils. (*K–M*) Spindle-like magnetofossils.

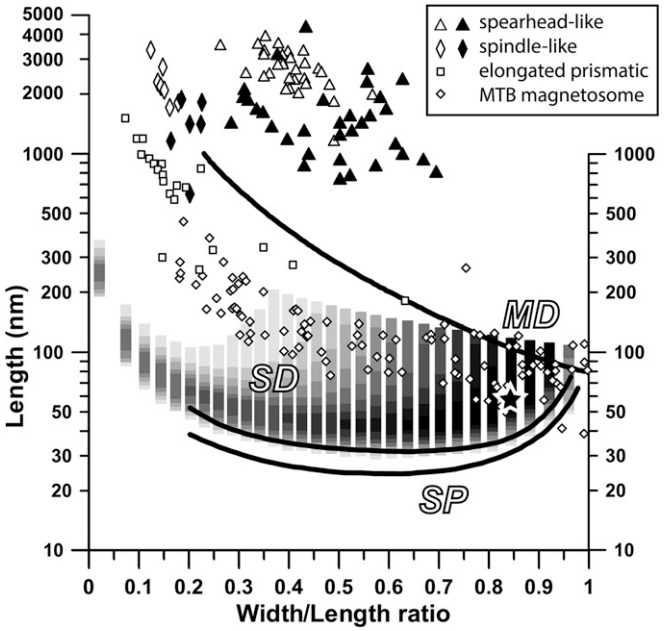

Fig. 4. Size-shape diagram of the giant magnetofossils and MTB magnetosomes. Solid and empty symbols represent data from this TXM study and previous SEM and TEM studies (9, 13), respectively. Triangles, rhombuses, and squares are spearhead-like, spindle-like, and elongated prismatic giant magnetofossils, respectively. Diamonds are magnetosomes produced by MTB. Lines define the size–shape ranges of superparamagnetic (SP), SD, and multidomain (MD) states for magnetite. Gray shades show the size–shape distribution of magnetites within the bulk CIE clay determined by thermal fluctuation tomography, with star indicating the peak concentration (6).

magnetite nanoparticles. However, previous rock magnetic studies, including thermal fluctuation tomography (shades in Fig. 4), first-order reversal curves, and ferromagnetic resonance spectra on the bulk CIE clay strongly suggest that most of the SD magnetite grains are isolated near-equant nanoparticles (6), rather than elongated prismatic crystals or magnetosome chains with significant shape anisotropy as hallmarks of biogenic origin. This is consistent with the only published TEM study on a bulk CIE clay sample (redeposited to a thin layer of ∼100-nm thickness), which found only a few isolated ∼50–70-nm magnetite grains but no shapes or chains ascribable to biogenic (5), because biogenic magnetite nanoparticles are known to be very difficult to disaggregate from their original chains (18).

In conclusion, along with previous rock magnetic and TEM studies, our quantitative constraints using ultrahigh-resolution synchrotron-based full-field X-ray microscopy suggest that the anomalously high SD magnetization of bulk CIE clay is dominated by isolated near-equidimensional magnetite nanoparticles, which are likely formed as vapor condensates inside an impact plume. Similar nanophase iron particles have been produced by pulse-laser irradiation of San Carlos Olivine with ∼9 wt% wustite (FeO) in the laboratory to simulate space weathering vapor redeposition by micrometeorite impacts (19). Iron-rich nanoparticles have also been detected with Mössbauer spectroscopy at several Cretaceous–Paleogene (K-Pg) boundary sites and are ascribed to condensates from an impact ejecta plume of the K-Pg asteroid (20). Our analogous results for the nonbiogenic SD magnetites in the CIE clay support the comet impact hypothesis as the trigger of the global environmental changes across the Paleocene–Eocene boundary.

Methods

The TXM used in this study is located at beamline X8C at the National Synchrotron Light Source (NSLS) at Brookhaven National Laboratory (BNL). We used the high-resolution imaging mode with a field-of-view of 20 μm × 20 μm. Large mosaic TXM images are stitched from multiple field-of-view images. To study the iron minerals within the clay, we used X-ray energy of 7.2 keV, just above the iron absorption K-edge (7.112 keV) (21), to allow maximum X-ray absorption. We used epoxy (almost X-ray–transparent) to secure the submillimeter bulk clay dusts on WC pins with tips of ∼50 μm. For each sample, its WC pin was mounted on a kinematic sample holder to be placed on a stage with motion of *x*, *y*, and *z* translations and rotation.

We first scanned submillimeter-sized CIE bulk clay dusts using a fast mosaic mode with 8 × 8 binning pixels (each pixel size is 10 nm) to cover the entire clay dust (Fig. 1*A*). Then, we used a slower but higher-resolution mosaic mode with 2 × 2 binning pixels to scan a smaller area of interest (Fig. 1*B*). For 3D tomographic studies, we took 721–1,081 images for each tomography with 20-μm target area in high-resolution mode (∼30–50 nm) from angles between 0° and 180°.

For the magnetically extracted materials from the CIE clay and the extract residues, we mounted them in clusters on steel pins for overall mosaic scans (Figs. S4 and S5). We then redeposited a thin layer of magnetically extracted materials on a Kapton tape (almost X-ray–transparent) by using an alcohol solution and mounted the tape on the sample stage perpendicular to the X-ray beam using a steel plate with openings and clips for further mosaic scans in a high-resolution mode with 2 × 2 binning pixels (Fig. 2).

For the freeze-dried MTB strain MV-1, we redeposited the samples in an alcohol solution on an SN window of 50-nm thickness (nearly X-ray–transparent) to allow minimum and homogeneous background X-ray absorption from the window, which introduced minimum background-imaging noise to the sample. We mounted the SN window perpendicular to the X-ray beam and used the ultrahigh-resolution mode without binning pixels for a resolution of one pixel size of 10 nm (Fig. S6). Only ∼micron-sized particles are identified, which may be derived from the ferric quinate used in the culture or hydrous ferric oxides that are precursors to magnetite precipitation (16).

For the redeposited bulk CIE clay, we suspended 60 mg of clay in 9 g (or ∼11.5 mL) of pure isopropyl alcohol. After shaking them well, we deposited a drop of the clay suspension (∼0.03 mL) on a 5-mm × 5-mm SN window. Based on the estimated clay density of 1.6 g/cm^3, we calculated that the redeposited and naturally dried clay layer has an average thickness of 4 μm. We took 1,370 X-ray images in the ultrahigh-resolution mode of single-pixel resolution and 20-μm × 20-μm field of view, which added up to a total scanned area of 0.55 mm^2 (volume of 2.2 × 10^{-3} mm^3 or weight of 3.5 μg of bulk clay).

ACKNOWLEDGMENTS. We thank Bruce M. Moskowitz (Institute for Rock Magnetism, University of Minnesota) for the MV-1 sample and Joseph L. Kirschvink (California Institute of Technology) for discussions on giant magnetofossils and MTB. We also thank Michael Winklhofer (Ludwig Maximilians University of Munich) and one anonymous reviewer for constructive comments. Use of the NSLS at BNL is supported by the United States Department of Energy, Basic Energy Sciences program, under Contract DE-AC02-98CH10886. Additional funding for this work was provided by the Rutgers Board of Governors Professor Research Fund. This is Contribution 7932 from the Lamont–Doherty Earth Observatory.

1. Kennett JP, Stott LD (1991) Abrupt deep-sea warming, palaeoceanographic changes and benthic extinctions at the end of the Palaeocene. *Nature* 353(6341):225–229.
2. Koch PL, Zachos JC, Gingerich PD (1992) Correlation between isotope records in marine and continental carbon reservoirs near the Paleocene Eocene boundary. *Nature* 358(6384):319–322.
3. Zachos JC, Lohmann KC, Walker JCG, Wise SW (1993) Abrupt climate change and transient climates during the Paleogene: A marine perspective. *J Geol* 101(2):191–213.
4. Lanci L, Kent DV, Miller KG (2002) Detection of Late Cretaceous and Cenozoic sequence boundaries on the Atlantic coastal plain using core log integration of magnetic susceptibility and natural gamma ray measurements at Ancora, New Jersey. *J Geophys Res* 107(B10):2216.
5. Kent DV, et al. (2003) A case for a comet impact trigger for the Paleocene/Eocene thermal maximum and carbon isotope excursion. *Earth Planet Sci Lett* 211(1-2):13–26.
6. Wang H, Kent DV, Jackson MJ (2013) Evidence for abundant isolated magnetic nanoparticles at the Paleocene-Eocene boundary. *Proc Natl Acad Sci USA* 110(2):425–430.
7. Wright JD, Schaller MF (2013) Evidence for a rapid release of carbon at the Paleocene-Eocene thermal maximum. *Proc Natl Acad Sci USA* 110(40):15908–15913.
8. Cramer BS, Kent DV (2005) Bolide summer: The Paleocene/Eocene thermal maximum as a response to an extraterrestrial trigger. *Palaeogeogr Palaeocl* 224(1-3):144–166.
9. Kopp RE, et al. (2007) Magnetofossil spike during the Paleocene-Eocene thermal maximum: Ferromagnetic resonance, rock magnetic, and electron microscopy evidence from Ancora, New Jersey, United States. *Paleoceanography* 22(4):PA4103.

10. Lippert PC, Zachos JC (2007) A biogenic origin for anomalous fine-grained magnetic material at the Paleocene-Eocene boundary at Wilson Lake, New Jersey. *Paleoceanography* 22(4):PA4104.
11. Chang L, et al. (2012) Giant magnetofossils and hyperthermal events. *Earth Planet Sci Lett* 351:258–269.
12. Kopp RE, et al. (2009) An Appalachian Amazon? Magnetofossil evidence for the development of a tropical river-like system in the mid-Atlantic United States during the Paleocene-Eocene thermal maximum. *Paleoceanography* 24(4):PA4211.
13. Schumann D, et al. (2008) Gigantism in unique biogenic magnetite at the Paleocene-Eocene Thermal Maximum. *Proc Natl Acad Sci USA* 105(46):17648–17653.
14. Wang J, et al. (2012) Automated markerless full field hard x-ray microscopic tomography at sub-50 nm 3-dimension spatial resolution. *Appl Phys Lett* 100:143107.
15. Witt A, Fabian K, Bleil U (2005) Three-dimensional micromagnetic calculations for naturally shaped magnetite: Octahedra and magnetosomes. *Earth Planet Sci Lett* 233(3-4):311–324.
16. Bazylinski DA, Frankel RB, Jannasch HW (1988) Anaerobic magnetite production by a marine, magnetotactic bacterium. *Nature* 334(6182):518–519.
17. Dunlop DJ, Özdemir Ö (2001) *Rock Magnetism: Fundamentals and Frontiers* (Cambridge Univ Press, Cambridge, UK).
18. Mann S, Sparks NHC, Walker MM, Kirschvink JL (1988) Ultrastructure, morphology and organization of biogenic magnetite from sockeye salmon, Oncorhynchus nerka: Implications for magnetoreception. *J Exp Biol* 140:35–49.
19. Sasaki S, Nakamura K, Hamabe Y, Kurahashi E, Hiroi T (2001) Production of iron nanoparticles by laser irradiation in a simulation of lunar-like space weathering. *Nature* 410(6828):555–557.
20. Wdowiak TJ, et al. (2001) Presence of an iron-rich nanophase material in the upper layer of the Cretaceous-Tertiary boundary clay. *Meteorit Planet Sci* 36(1):123–133.
21. Baker DR, et al. (2012) An introduction to the application of X-ray microtomography to the three-dimensional study of igneous rocks. *Lithos* 148:262–276.

Supporting Information

Wang et al. 10.1073/pnas.1517475112

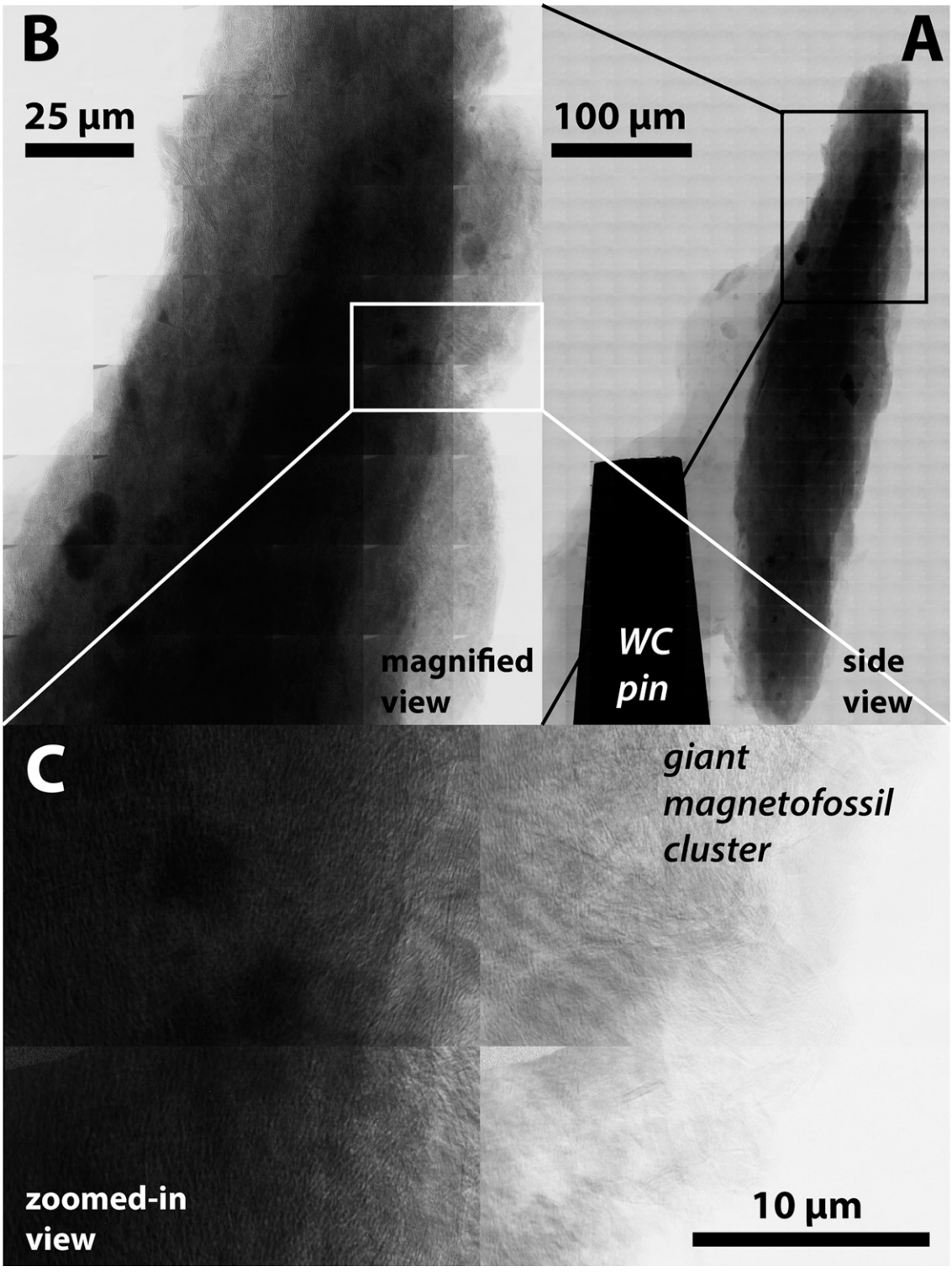

Fig. S1. (*A*) TXM mosaic scan of the side view (rotated 90° from the front view) of the submillimeter bulk CIE clay dust AN560.1-X1 by fast mode. (*B*) Slow mosaic mode scan of the boxed area in *A*. (*C*) Magnified view of the boxed area in *B*.

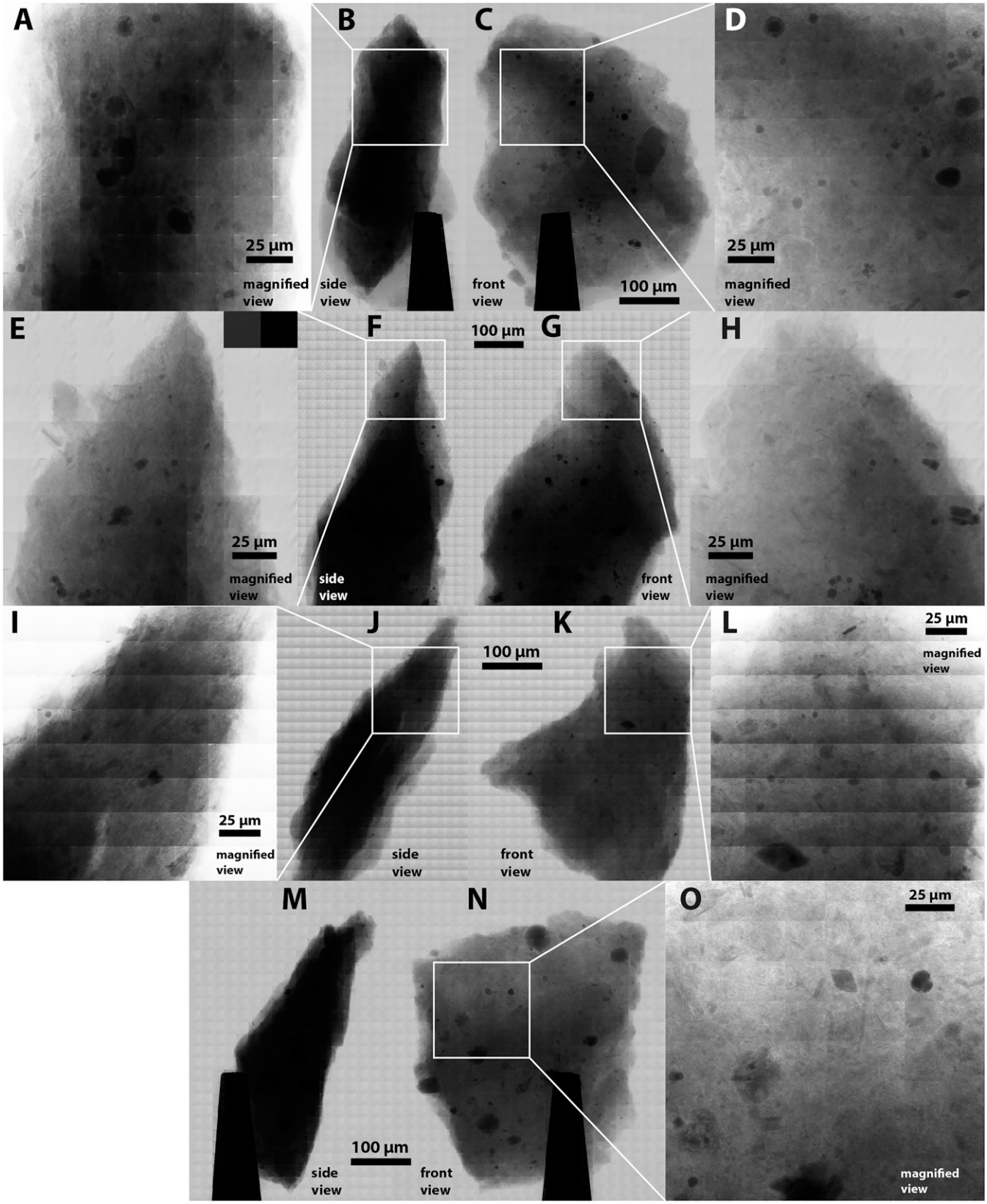

Fig. S2. (*A–O*) TXM mosaic scans of the front and side view of four extra submillimeter bulk CIE clay dusts from AN560.1 by fast mode with slow mosaic mode scans showing the areas in the boxes. Similar iron minerals can be identified as in AN560.1-X1 (Fig. 1 and Fig. S1).

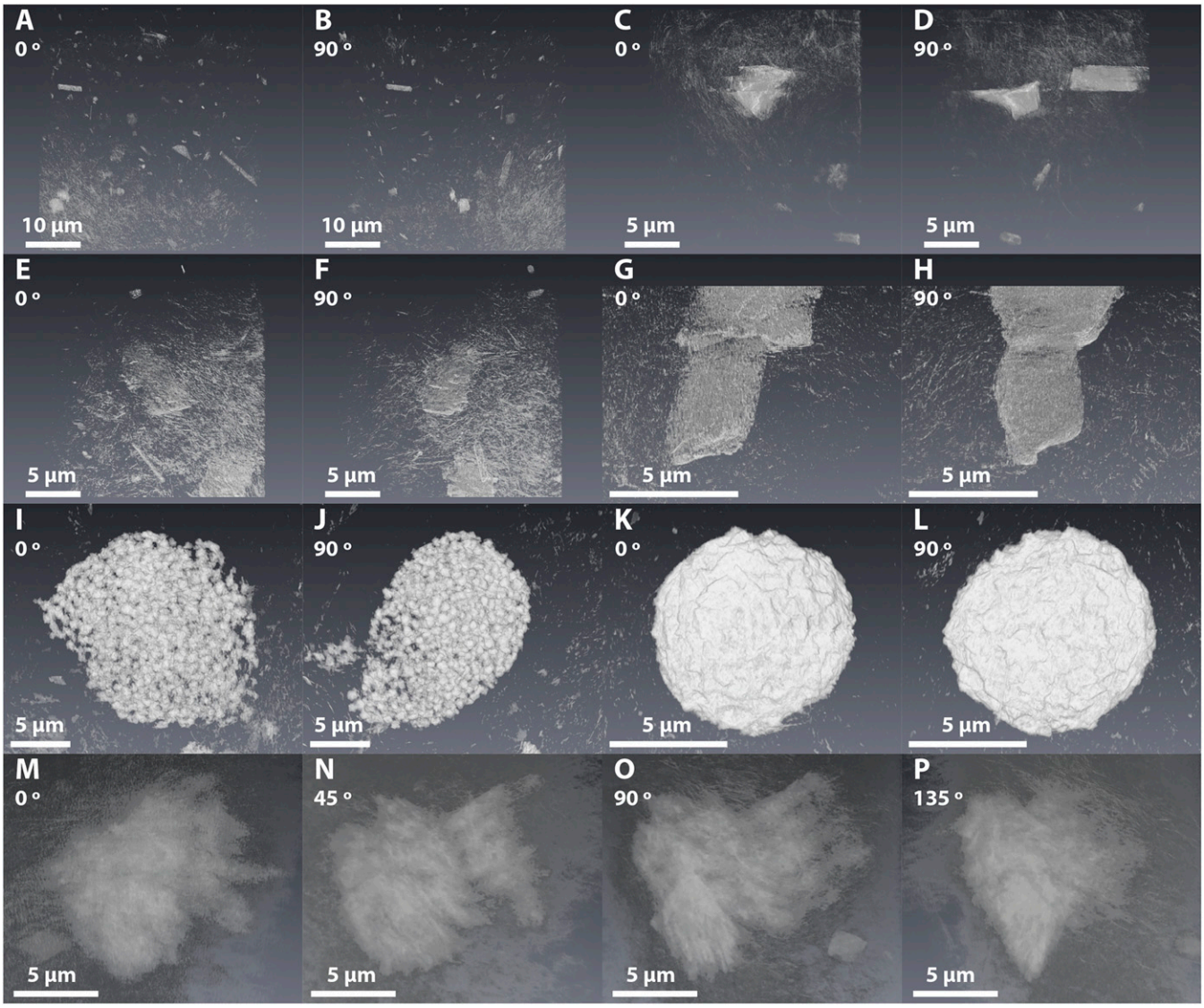

Fig. S3. Three-dimensional TXM tomographic reconstructions viewed from different angles as indicated on each image. Brightness is inverted in 3D reconstructions with brighter meaning greater X-ray absorption and higher iron concentration. (*A*–*H*) Several areas containing detrital iron mineral grains. (*I*–*L*) Pyrite framboids. (*M*–*P*) A possible magnetofossil cluster of the creature that produced spindle-like magnetite crystals in its original state. Corresponding 3D structures viewed from 0° to 360° are shown in Movies S1–S7.

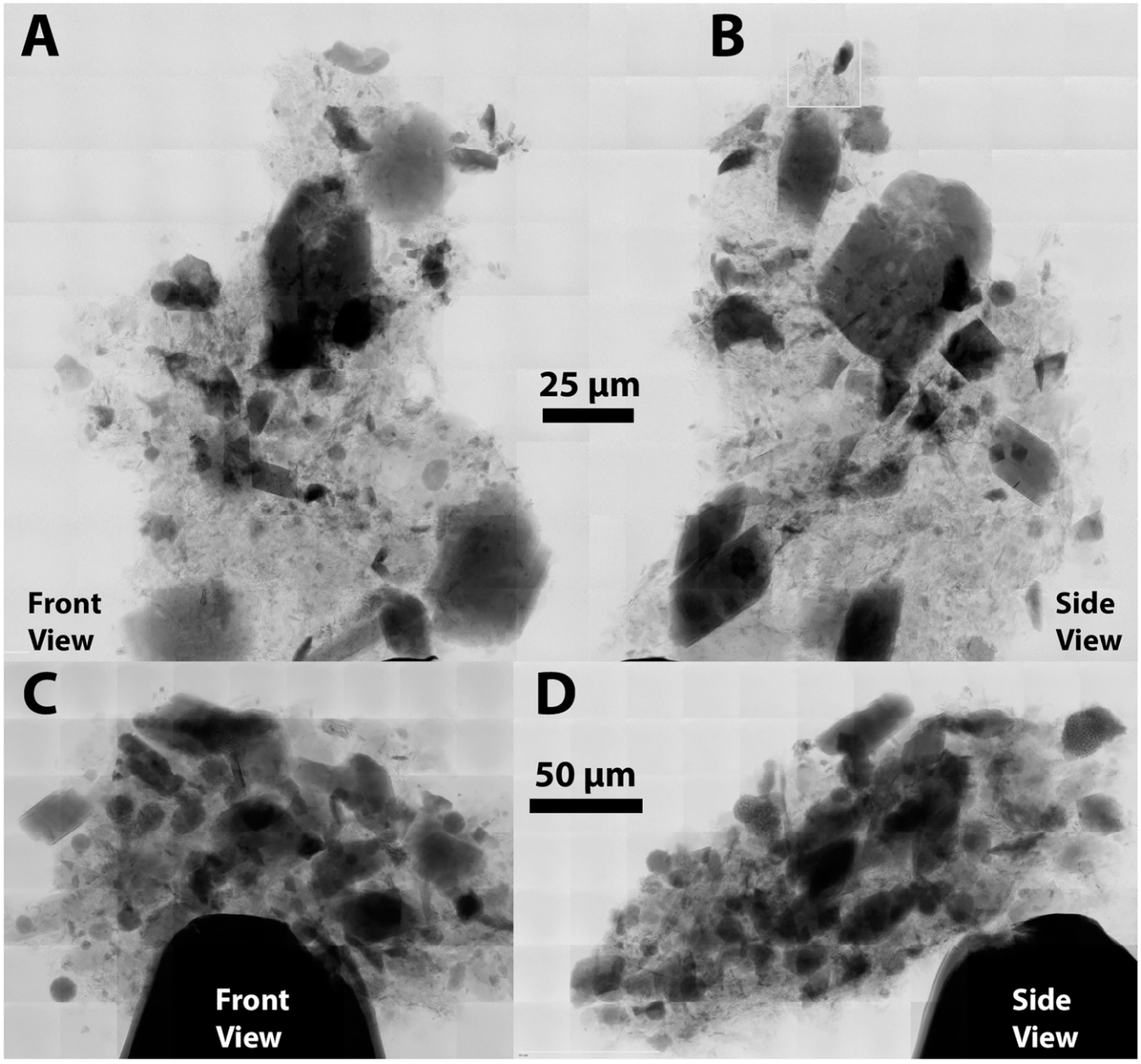

Fig. S4. TXM mosaic scans of cluster-1 (*A* and *B*) and cluster-2 (*C* and *D*) of magnetically extracted materials from AN560.1.

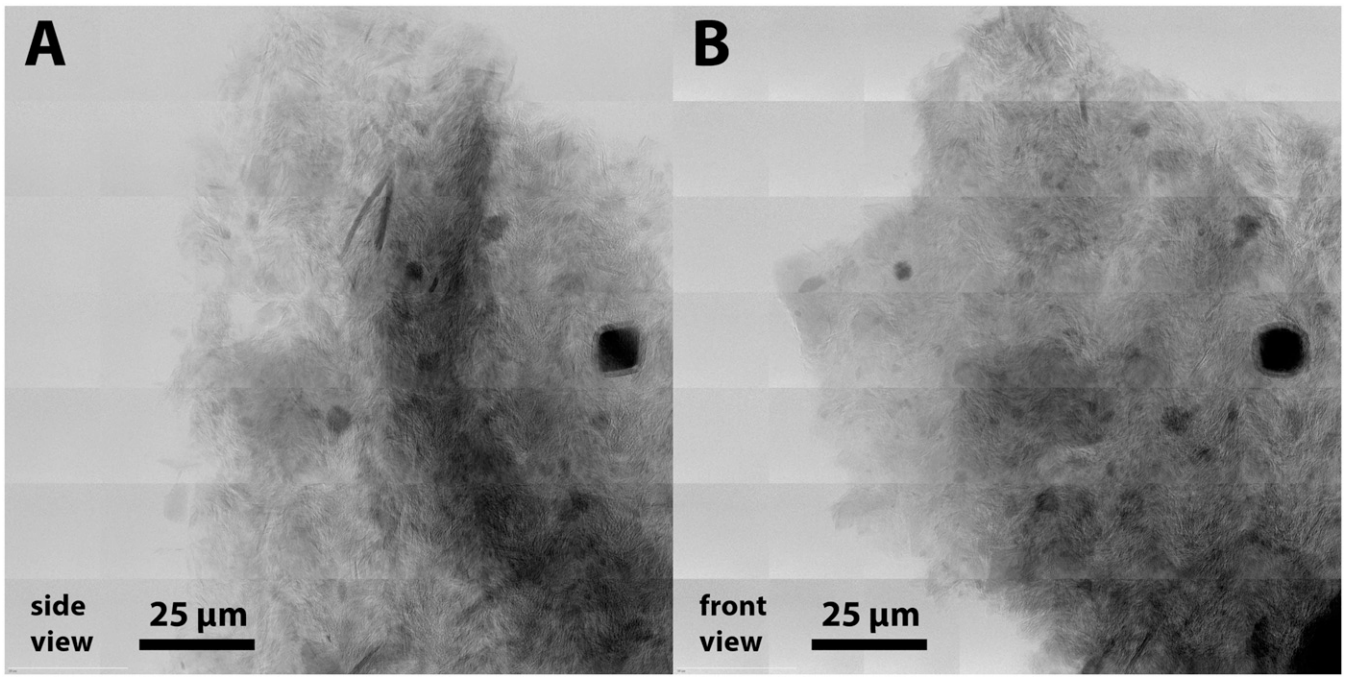

Fig. S5. TXM mosaic scans of a magnetic extract residue of AN560.1. (*A*) Side view. (*B*) Front view.

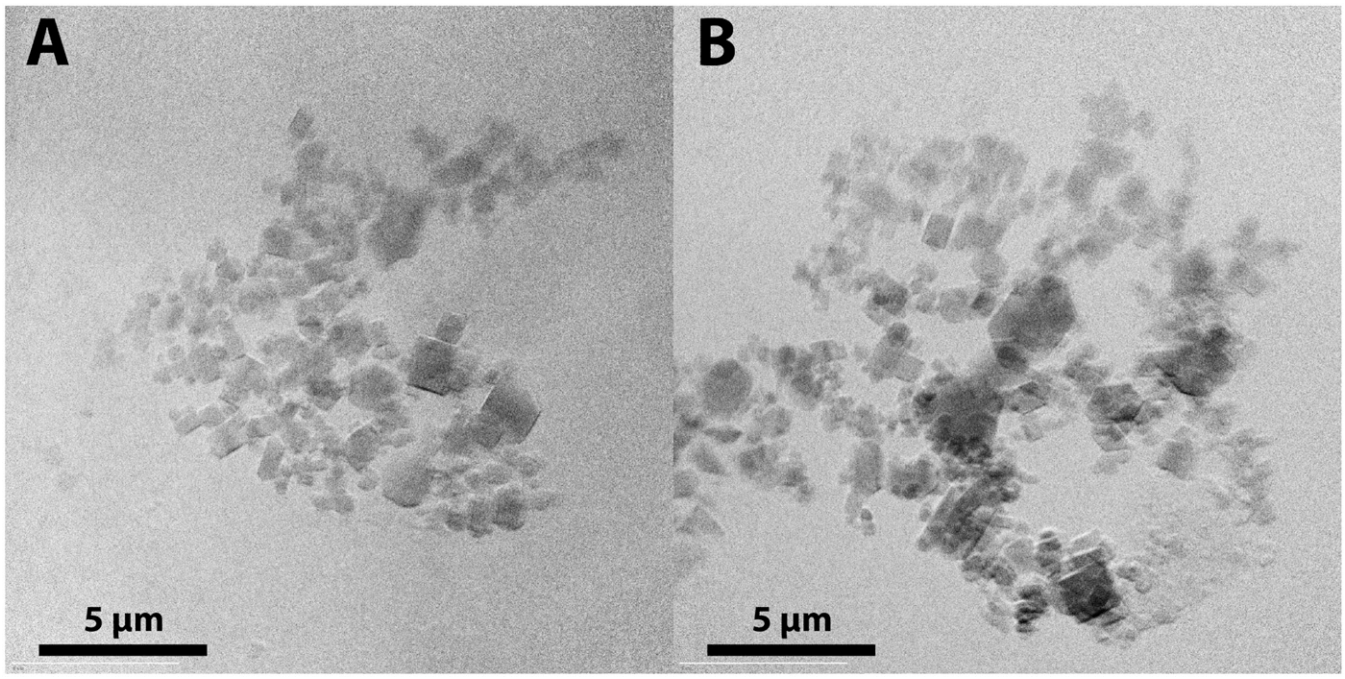

Fig. S6. (*A* and *B*) TXM images of two clusters of freeze-dried cultured MTB strain MV-1.

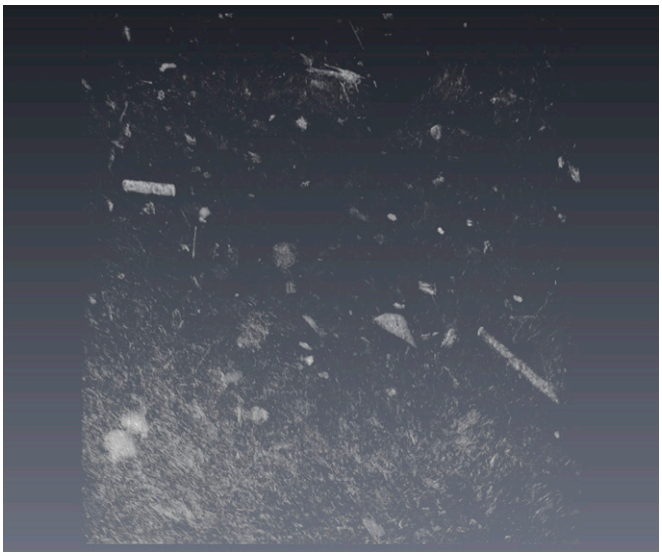

Movie S1. TXM tomographic 3D reconstruction of an area containing detrital iron mineral grains viewed from 0° to 360° as shown in Fig. S3 *A* and *B*.

Movie S1

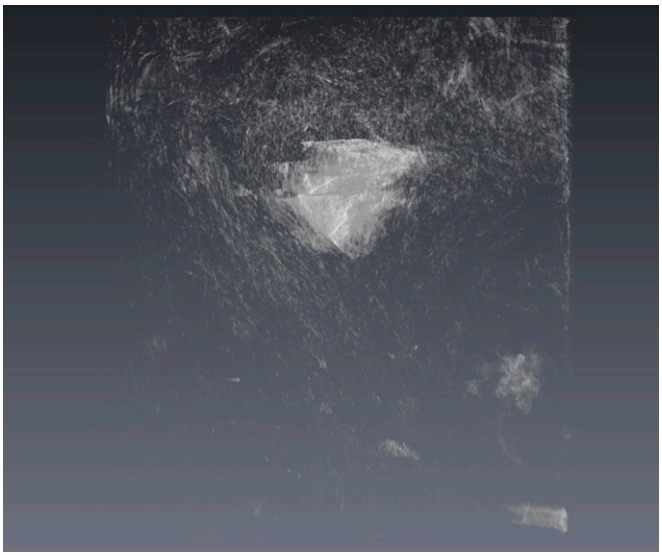

Movie S2. TXM tomographic 3D reconstruction of an area containing detrital iron mineral grains viewed from 0° to 360° as shown in Fig. S3 *C* and *D*.

Movie S2

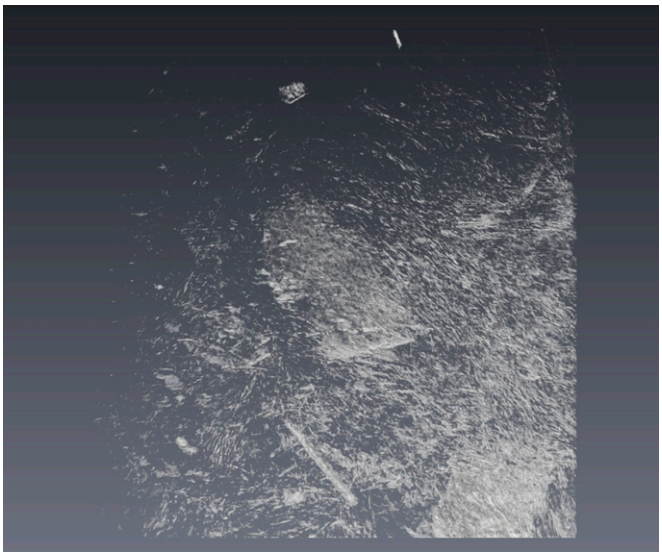

Movie S3. TXM tomographic 3D reconstruction of an area containing detrital iron mineral grains viewed from 0° to 360° as shown in Fig. S3 *E* and *F*.

Movie S3

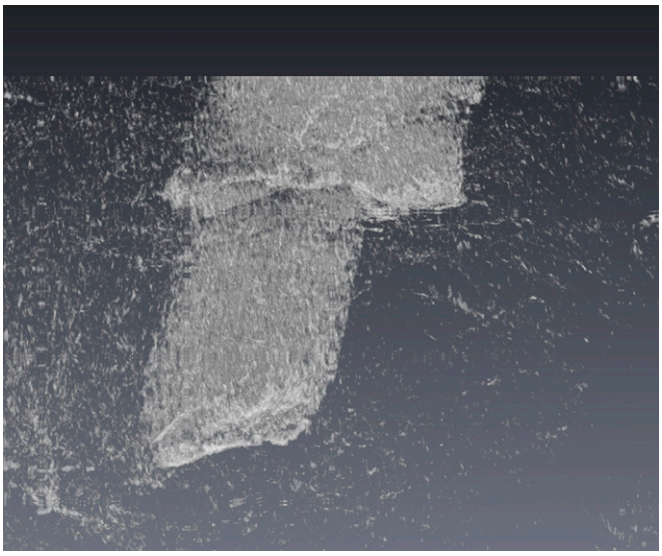

Movie S4. TXM tomographic 3D reconstruction of an area containing detrital iron mineral grains viewed from 0° to 360° as shown in Fig. S3 *G* and *H*.

Movie S4

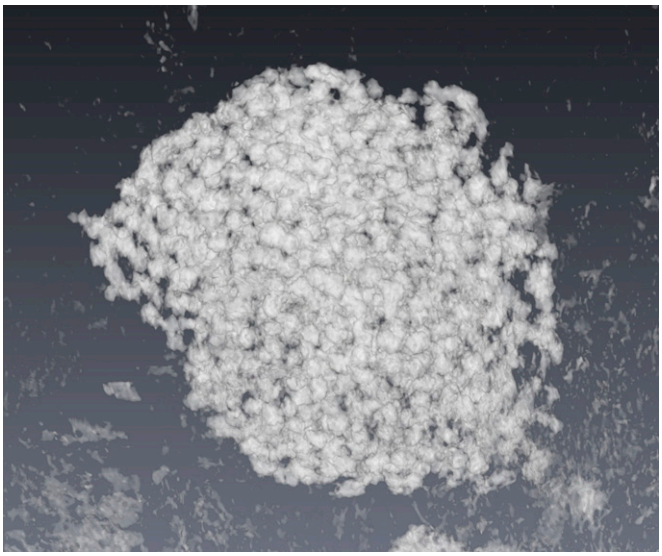

Movie S5. TXM tomographic 3D reconstruction of a pyrite framboid viewed from 0° to 360° as shown in Fig. S3 *I* and *J*.

Movie S5

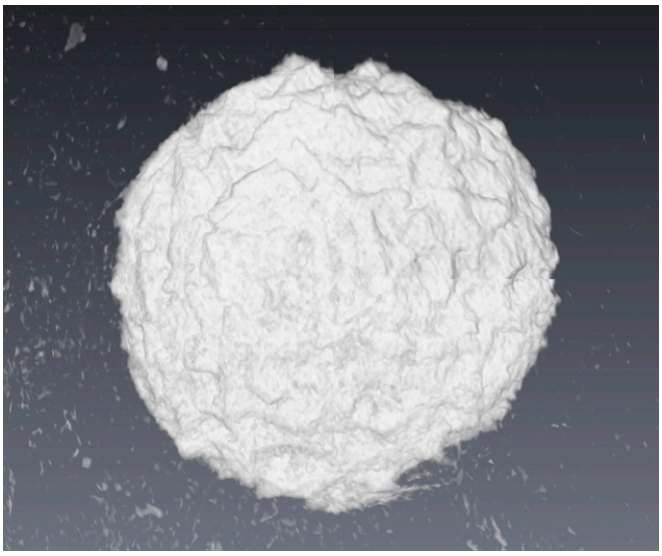

Movie S6. TXM tomographic 3D reconstruction of a pyrite framboid viewed from 0° to 360° as shown in Fig. S3 *K* and *L*.

Movie S6

Movie S7. TXM tomographic 3D reconstruction of a possible magnetofossil cluster of the creature that produced spindle-like magnetite crystals in its original state viewed from 0° to 360° as shown in Fig. S3 *M* to *P*.

Movie S7